Floquet Engineering Topological Dirac Bands

Mingwu Lu, G. H. Reid, A. R. Fritsch, A. M. Piñeiro, and I. B. Spielman*
Joint Quantum Institute, National Institute of Standards and Technology, and University of Maryland, Gaithersburg, Maryland 20899, USA

(Received 16 February 2022; revised 25 May 2022; accepted 22 June 2022; published 22 July 2022)

We experimentally realized a time-periodically modulated 1D lattice for ultracold atoms featuring a pair of linear bands, each with a Floquet winding number. These bands are spin-momentum locked and almost perfectly linear everywhere in the Brillouin zone: a near-ideal realization of the 1D Dirac Hamiltonian. We characterized the Floquet winding number using a form of quantum state tomography, covering the Brillouin zone and following the micromotion through one Floquet period. Last, we altered the modulation timing to lift the topological protection, opening a gap at the Dirac point that grew in proportion to the deviation from the topological configuration.

DOI: 10.1103/PhysRevLett.129.040402

Topologically protected edge modes are present in systems from 2D and 4D quantum Hall systems [1,2], Z_2 topological insulators [3], to atmospheric waves [4]. Time-periodic driving, described by Floquet theory, allows for new topological invariants [5–7] including the Floquet winding number, leading to new protected quantities. Here, we study atomic Bose-Einstein condensates (BECs) in the lowest two bands of a periodically driven 1D optical lattice and observe a pair of protected chiral bands that are a near-ideal realization of the 1D Dirac Hamiltonian. We extract the topological winding number from the time-resolved micromotion and find that altering the modulation timing opens a gap at the Dirac point.

The bulk-edge correspondence yields protected edge bands that reside on the system's surface. For example, 2D-Z_2 topological insulators have a pair of counterpropagating spin-momentum locked 1D edge modes. By contrast we observe 1D topologically protected bands derived from a periodically driven 1D system, where the topological protection results from a nonzero Floquet winding number [5] defined in terms of the $1+1$D space defined by crystal momentum q and time t [8]. These bands are spin-momentum locked, intersect at $q=0$, and have the remarkable property of being linear everywhere in the Brillouin zone (BZ). The periodic quasienergy structure of Floquet systems allows these bands to smoothly cross the edge of the BZ by entering the next quasienergy zone.

All of these features are present in a periodically modulated Su-Schrieffer-Heeger (SSH) model [9]

$$\hat{H} = -\sum_j [J|j+1,\downarrow\rangle\langle j,\uparrow| + J'|j,\downarrow\rangle\langle j,\uparrow| + \text{H.c.}]$$

that approximates our 1D bipartite lattice [10]. Each unit cell (labeled by integer j) consists of sites that we denote by $|\uparrow\rangle$ and $|\downarrow\rangle$ to emphasize their role as a pseudospin degree of freedom [Fig. 1(a)]. J' and J are the tunneling strengths within a unit cell and between adjacent unit cells, respectively.

Following Ref. [8], we implemented a Floquet "switching" protocol where the lattice periodically alternates between a configuration I (C-I) with $J' \approx 0$ and $J = J_0$ and a reversed configuration II (C-II) with period T. This allows intercell tunneling $|j+1,\downarrow\rangle \leftrightarrow |j,\uparrow\rangle$ during the first half period and intracell tunneling $|j,\downarrow\rangle \leftrightarrow |j,\uparrow\rangle$ during the second half period. When $J_0 T = \pi$ each half period implements a π pulse, exchanging the amplitude between sites. Figure 1(a) illustrates how this leads to a displacement of the lattice constant a per Floquet period, with $|j,\uparrow\rangle \to |j+1,\uparrow\rangle$ and $|j,\downarrow\rangle \to |j-1,\downarrow\rangle$. This gives constant velocity $v = \pm a/T$, (pseudo)spin-momentum locked motion under stroboscopic observation. Together these features are captured by a 1D Floquet Dirac Hamiltonian $\hat{H}^F(q) = qv\hat{\sigma}_z$ describing massless (i.e., gapless) relativistic particles [8]. Any deviation from exact π pulses opens gaps in the quasienergy spectrum $\hbar\epsilon_\alpha(q)$, where α labels the quasienergy band. For each initial pseudospin, different crystal momentum states start and end each driving period at the same point on the Bloch sphere, but follow different trajectories. We show that, taken over the whole BZ, these trajectories cover the Bloch sphere, giving winding numbers of ± 1 for initial pseudospins $|\uparrow\downarrow\rangle$. A related experiment in a small synthetic dimension chain observed the drift of initially localized states [12] but neither the linear drift of crystal momentum eigenstates nor the band topology.

Experiments.—Our experiments began with small $N \approx 10^4$ atom [13] ^{87}Rb BECs in a crossed optical dipole trap (ODT) in the $|f=1, m_F=-1\rangle$ hyperfine ground state. The ODT, formed by two intersecting 1064 nm laser beams traveling along $\mathbf{e}_x$ and $\mathbf{e}_y$, had trap frequencies $(\omega_x, \omega_y, \omega_z)/2\pi \approx (15, 150, 100)$ Hz. A bias magnetic

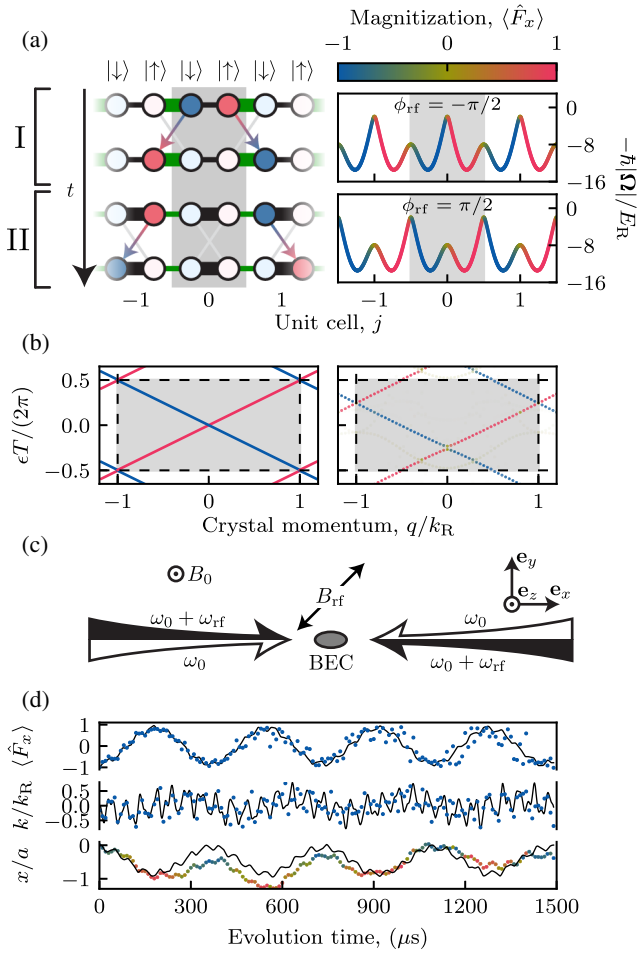

FIG. 1. Concept. (a) Left: switching protocol, with the $j = 0$ unit cell marked in gray. In C-I atoms tunnel between neighboring unit cells (bold green links); in C-II, they tunnel within the same unit cell (bold black links). Right: adiabatic lattice potentials colored by $\langle \hat{F}_x \rangle$. (b) Floquet band structure colored according to $\langle \hat{F}_x \rangle$ sampled stroboscopically. The lowest BZ and quasienergy zone is marked in gray. Left: idealized SSH model. Right: numerical lattice model [11]. (c) Schematic. The BEC was illuminated by counterpropagating Raman lasers and an radio frequency (rf) magnetic field. (d) Static lattice tunneling with data (markers) and simulations (black curves). Upper: magnetization $\langle \hat{F}_x \rangle$. Middle: group velocity. Bottom: displacement colored according to $\langle \hat{F}_x(t) \rangle$ using the color scale in (a).

field $B_0 \approx 0.1$ mT Zeeman split the three m_F states by $\omega_Z/2\pi \approx 1$ MHz. These states were dressed by a rf magnetic field with frequency $\omega_{\rm rf}$ and two laser beams counterpropagating along $\mathbf{e}_x$ driving Raman transitions. As shown in Fig. 1(c), each Raman beam had frequency components ω_0 and $\omega_0 + \omega_{\rm rf}$; $\phi_{\rm rf}$ denotes the relative phase between the rf field and the Raman beat tone. The wavelength $\lambda_R = 2\pi c/\omega_0 = 790.03(2)$ nm of the Raman lasers [15] defines the single-photon recoil wave vector $k_R = 2\pi/\lambda_R$ and energy $E_R = \hbar^2 k_R^2/2m$, with speed of light c and reduced Planck constant $\hbar$. The atoms interact with these fields via a Zeeman-like Hamiltonian [16] $\hat{H}_{\rm int} = \mathbf{\Omega}(\hat{x}) \cdot \hat{\mathbf{F}}$, with total atomic angular momentum operator $\hat{\mathbf{F}}$. The effective magnetic field $\mathbf{\Omega}(\hat{x}) = [\Omega_{\rm rf}\cos(\phi_{\rm rf}) + \bar{\Omega}\cos(2k_R\hat{x}), -\Omega_{\rm rf}\sin(\phi_{\rm rf}) - \delta\Omega\sin(2k_R\hat{x}), \sqrt{2}\delta]/\sqrt{2}$ is defined in terms of the detuning $\delta = \omega_Z - \omega_{\rm rf}$; the rf coupling strength $\Omega_{\rm rf}$; and $\bar{\Omega} = \Omega_+ + \Omega_-$ and $\delta\Omega = \Omega_+ - \Omega_-$, derived from the two Raman coupling strengths $\Omega_\pm$. The lowest energy adiabatic potential formed a spin-dependent bipartite lattice [10], shown for two choices of $\phi_{\rm rf}$ in Fig. 1(a). As indicated by the magnetization of the adiabatic potentials, the $|\uparrow,\downarrow\rangle$ sites are highly spin polarized, corresponding to atomic states $|m_x = \pm 1\rangle$. The potential minima are degenerate for $\phi_{\rm rf} = \mp \pi/2$, where $\mp$ selects between C-I and C-II. All other values of $\phi_{\rm rf}$ introduce an energy difference Δ between $|\uparrow,\downarrow\rangle$ that, while absent in the SSH model, is useful for state preparation [11] and readout.

Following all our experiments, we measured the spin-resolved momentum distribution by first removing the Raman lasers and the rf field. An rf pulse induced a $\pi/2$ rotation around $\hat{F}_y$, transforming eigenstates of $\hat{F}_x$ to our $\hat{F}_z$ measurement basis; we then initiated time of flight (TOF) by extinguishing the trapping lasers. During the 12 ms TOF a magnetic field gradient along $\mathbf{e}_y$ Stern-Gerlach separated the three m_F states, after which the density distribution was resonantly absorption imaged. This allowed us to separately infer the overall populations in the $|\uparrow\rangle, |\downarrow\rangle$ sites.

Our procedure for loading BECs into the bipartite lattice adiabatically ramped the coupling fields and detuning to their final values in 2.5 ms, with $\phi_{\rm rf} = 0$ or π chosen to select occupation on $|\uparrow\rangle$ or $|\downarrow\rangle$ sites. Last, we selected between C-I and C-II by abruptly changing $\phi_{\rm rf}$ to $\mp \pi/2$. The resulting $q = 0$ pseudospin polarized state was an equal superposition of our lattice's lowest two bands; following loading, atoms resonantly tunneled between the strongly coupled neighboring pseudospins [17,18].

Dispersion.—Figure 1(d) plots this tunneling in C-I for atoms prepared in $|\downarrow\rangle$ where data is plotted by markers and the solid curves are the results of our numerical model [19]. The top panel shows the measured magnetization $\langle \hat{F}_x \rangle$ coherently oscillating with 366(3) μs period, resulting from motion between neighboring sites. We separately observe near-zero population in $|m_x = 0\rangle$ during this evolution, enabling the mapping $|\uparrow,\downarrow\rangle \to |m_x = \pm 1\rangle$. The scatter increases at long times, indicating the onset of dephasing, likely from a combination of optical path changes from acoustic vibrations, laser intensity noise, and magnetic field instabilities.

Figure 1(d), (middle) plots the instantaneous group velocity obtained from the momentum distribution measured in TOF [20]. The high frequency oscillations are repeatable and have amplitude consistent with the ≈7% occupation of higher bands anticipated by our numerical

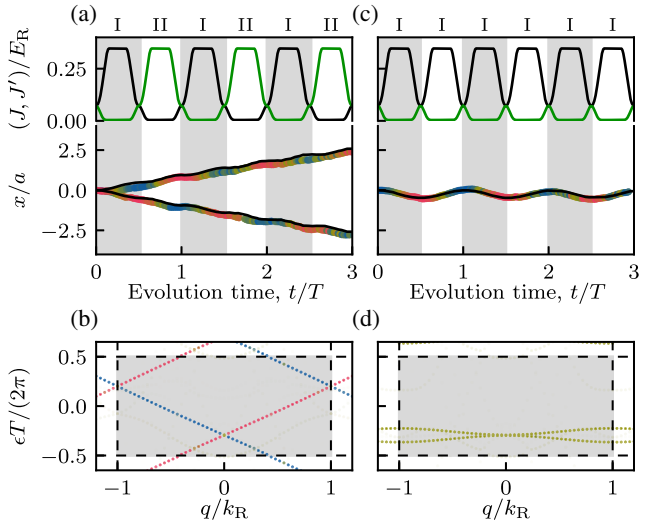

FIG. 2. Floquet protocols. (a),(b) switching protocol and (c),(d) the single-configuration protocol. (a),(c) Computed intercell (black) and intracell (green) tunneling strengths and displacement (colored according $\langle \hat{F}_x \rangle$). Gray and white bands indicate the different configurations. (b),(d) Floquet quasienergies [using the same color scale as in Fig. 1(a)].

modeling (black). The bottom panel integrates the group velocity [21], giving the BEC's displacement as it tunnel oscillates between adjacent lattice sites separated by nearly $1/2$ of a unit cell, $\approx$200 nm. While the higher frequency components are conspicuous in group velocity, they play little role in atomic displacement at the tunneling timescale, since integration acts as a low-pass filter.

Having demonstrated the behavior of the static lattice, Fig. 2(a) depicts the configuration switching protocol with near optimal timing. This was achieved by suddenly changing the phase ϕ_{rf}, ideally every half tunneling period as evoked in Fig. 1(a). To avoid exciting higher bands with these abrupt switches, we smoothly ramped Ω_{rf} to zero, changed ϕ_{rf}, and reversed the ramp, smoothly changing J and J' as in the Fig. 2(a), (top). The drive period $T = 448\ \mu$s increased from the $\approx$366 μs bare tunneling period [Fig. 1(d)], resulting from the time spent ramping Ω_{rf} to and from zero, during which time tunneling was suppressed. We empirically found the rf phases to achieve C-I and C-II differed by $\phi_{\mathrm{rf}}^{(\mathrm{II})} - \phi_{\mathrm{rf}}^{(\mathrm{I})} \approx 1.03\pi$ rather than π as predicted by our model. In addition, we observed a 6(2)% difference in their tunneling periods [22]. We compensated for this in our modulation scheme by reducing the time spent in C-II proportionally.

Figure 2(a), (bottom) shows results for atoms prepared in $|\uparrow\rangle$ (positive slope) and $|\downarrow\rangle$ (negative slope). Following each Floquet period, the magnetization of both trajectories (indicated by the color of the markers), returned to their initial values, demonstrating spin-momentum locking of Floquet eigenstates. These data show a near-linear increase of displacement sustained over many Floquet periods consistent with our numerically modeled time evolution (black), yielding drift velocities $\pm 0.89(4)a/T$ and $\pm 0.86(2)a/T$, respectively. These differ from the ideal drift velocity a/T, i.e., one unit cell per cycle that is representative of the overall slope of the band structure [Fig. 2(b)]. Our numerics indicate this results from the nonzero value of both J and J' during our rf-switching stage [black and green curves in Fig. 2(a), (top)], allowing unwanted tunneling; and the departure of our physical system from the tight-binding SSH model. Nevertheless, our numerics indicate that the group velocity averaged over the BZ has magnitude a/T for each band.

To confirm the importance of the configuration-switching protocol, we introduced a single-configuration protocol with the same Ω_{rf} ramps but with constant ϕ_{rf} [Fig. 2(c)]. The displacement and magnetization measured following this protocol are oscillatory and correspond to tunneling confined within a single double well. Figure 2(d) shows the associated Floquet band structure with a quadratic touching point, reminiscent to those in bilayer graphene [23]. The curvature of these bands results from the same deviations described above for the configuration-switching protocol.

Winding number.—Similar to adiabatic pumps [24], the topology of 1D Floquet bands is characterized by an integer valued winding number

$$\nu = \frac{1}{2\pi} \int_{\mathrm{BZ}} \int_0^T dq dt F(q,t), \tag{1}$$

defined in terms of the Berry curvature $F(q,t) = (\langle \partial_q \psi(q,t) \rangle \partial_t \psi(q,t) - \mathrm{c.c.})/i$. We reconstruct the two component (pseudo-)spinor $|\psi(q,t)\rangle$ for all crystal momentum states over one period of modulation using quantum state tomography [25] and directly compute ν [26] using Ref. [27] for discretely sampled data.

Our standard measurement gives the population in the $\{|\uparrow\rangle, |\downarrow\rangle\}$ states from which we obtain $\langle \hat{\sigma}_z \rangle$. To measure $\langle \hat{\sigma}_x \rangle$ and $\langle \hat{\sigma}_y \rangle$, we designed lattice configurations for which evolution implemented pseudospin rotations generated by $(\hat{\sigma}_x + \hat{\sigma}_z)/\sqrt{2}$ and $\hat{\sigma}_x$, respectively [28]. We applied these operations after the system evolved for a time t and parallelized the measurement by filling the ground band of our initial lattice [29] to measure all q states simultaneously [30,31]. These data yielded the crystal momentum resolved pseudospin magnetization $\mathbf{m}(q,t) = (\langle \hat{\sigma}_x(q,t) \rangle, \langle \hat{\sigma}_y(q,t) \rangle, \langle \hat{\sigma}_z(q,t) \rangle)$ from the populations following each rotation. Figure 3(a) plots all three components of $\mathbf{m}(q,t)$ for a single Floquet cycle of our configuration-switching protocol, starting in state $|\uparrow\rangle$. Our experimental data (right) are consistent with numerical simulation (left).

Our measurement of $\mathbf{m}(q,t)$ suffices to obtain the associated Floquet winding number [5] using Eq. (1). Evaluating the Berry curvature requires differentiation of noisy data, so we applied a low-pass Gaussian filter (with root mean squared widths $\Delta t = 10\ \mu$s and $\Delta q = k_R/6$)

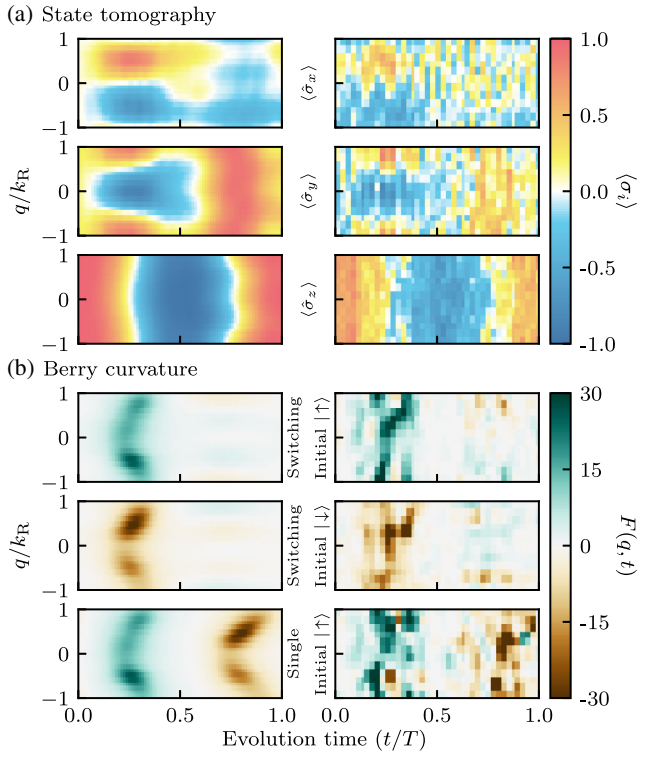

FIG. 3. Crystal momentum resolved pseudospin micromotion and corresponding Berry curvature. Upper three panels: Numerical model (left) and unfiltered experimental data (right) for pseudospin components for configuration switching protocol (initial states $|\uparrow\rangle$). Lower three panels: Berry curvature based on filtered experimental data (right) and numerical simulation (left) for configuration switching protocol with initial states $|\uparrow\rangle$ and $|\downarrow\rangle$ and single-configuration protocol (initial state $|\uparrow\rangle$).

prior to computing $F(q,t)$. Panel (b) plots the resulting Berry curvatures $F(q,t)$ for our configuration switching protocol with initial states $|\uparrow\rangle$ and $|\downarrow\rangle$, as well as our single-configuration protocol (top, middle, and bottom, respectively). For $|\uparrow\rangle$, $F(q,t)$ has a net positive contribution for $t < T/2$; while for $t > T/2$ both positive and negative structures are present; these cancel upon integration. All together we find $\nu_{\uparrow,\downarrow} = \{0.991(5), -0.998(4)\}$ for systems initialized in $|\uparrow\rangle$ or $|\downarrow\rangle$; this is in very good agreement with $\{0.9994, -0.9995\}$ obtained by performing the same analysis on numerically simulated data. Uncertainties in our lattice parameters (leading to deviations from optimal timing) and imperfect state preparation can cause the time evolution to be not perfectly T periodic, yielding noninteger ν even without the technical noise present in experiment. For comparison, panel (b) bottom shows $F(q,t)$ for our single-configuration protocol, for which we obtain $\nu = 0.01(2)$, compared to $\nu = 0.0019$ from simulation. Here, our initial state was fully magnetized, an eigenstate of the ideal switching protocol, but a coherent superposition of the two bands shown in Fig. 2(d).

Unlike topological invariants in static systems, the Floquet winding number is directly linked to $\epsilon_\alpha(q)$ via [5]

$$\nu = \sum_\alpha \left[\frac{T}{2\pi} \int_{\mathrm{BZ}} dq \partial_q \epsilon_\alpha(q) \right]. \tag{2}$$

Each term of the sum measures the difference in quasienergy at the $\pm$ edges of the BZ for the αth band; the integral is zero for bands that link at the edge of the BZ (such as our single-configuration protocol) since $\epsilon_\alpha(-k_R) = \epsilon_\alpha(k_R)$. By contrast our Dirac-like bands change in quasienergy by $\pm 2\pi/T$, each contributing ± 1 to the sum suggesting $\nu = 0$. Our configuration switching protocol leads to a pair of chiral symmetries [8] with symmetry operators $\{\hat{\sigma}_x, \hat{\sigma}_y\}$; for example, the symmetry operation $\hat{\Sigma} = \hat{\sigma}_x$ takes $\hat{\Sigma}^\dagger \hat{H}^{\mathrm{F}} \hat{\Sigma} = -\hat{H}^{\mathrm{F}}$. Together these separate state space into decoupled $\uparrow$ and $\downarrow$ subspaces that individually have $\nu_{\uparrow\downarrow} = \pm 1$. The quantization of the Floquet winding number results from the continuity of the Floquet band structure in the combined Bloch-Floquet BZ, even in the absence of chiral symmetry. In our case, chiral symmetry enables the Floquet winding number to take nonzero values.

Fine-tuning.—The chiral symmetry is present only for a fine-tuned switching protocol, i.e., tunneling π pulses as discussed above; for example, changing the tunneling period to $T_0 + \delta T$ open a gap $\approx 2J_0|\delta T|/T_0$ in the Floquet spectra at the center of the BZ [32] leading to nontopological bands with massive Dirac dispersion.

Figure 4(a) plots the time evolving position when $J_0 T < \pi$; the data are colored according to their instantaneous magnetization and the gray boxes mark the configurations. This shows the first switch occurring before the magnetization inverts, and at longer timescales the position undergoes periodic oscillations—zitterbewegung [33]—arising from the quantum interference [34] of the two gapped bands at $q = 0$, shown in Fig. 4(b).

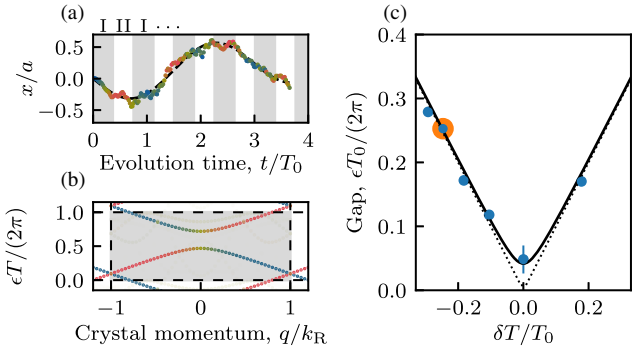

FIG. 4. Breaking of chiral symmetry. (a) Time evolution with Floquet period $T = 330\ \mu$s, away from the optimal point $T_0 = 438\ \mu$s, colored according to the instantaneous magnetization using the color scale in Fig 1. Configurations (gray rectangles) are plotted along with the data. (b) Computed spectrum for data in (a), and circled in orange in (c). (c) Zitterbewegung frequency as a function of $\delta T/T_0$ showing the gap closing at the symmetry point.

The dependence of the gap on δT in Fig. 4(c) is in near perfect agreement with the simple model (dashed lines), and fitting to a hyperbola provides an upper bound $0.05(1) \times (2\pi/T_0)$ of the gap in our fine-tuned configuration, indicating that our experiment was very close to the optimal configuration.

Discussion and outlook.—Topological systems can be organized by their symmetries [35], and the breaking of the chiral symmetry of our system is similar to Z_2 topological insulators where any small magnetic field breaks time reversal symmetry and opens a gap where the edge bands cross. In our case, perturbations to the *Floquet* Hamiltonian that obey the chiral symmetries leave the winding number unchanged; however, the linear dispersion would in general be lost. Such terms generally derive from time-dependent perturbations in the lab frame. This Floquet topological protection may have applications similar to dynamical decoupling [36] where suitable time-dependent driving renders Floquet systems immune to targeted noise. By contrast perturbations to the static Hamiltonian that obey the chiral symmetries generally lead to terms in the Floquet Hamiltonian that do not obey chiral symmetry.

Our protocol realizes a diabatic quantized pump, complementing adiabatic topological and geometrical adiabatic Thouless pumps [24] realized with ultracold atoms [10,37–39] as well as proposals for high frequency topological pumps [40,41]. Adiabatic Thouless pumps are also characterized by the Floquet topological index in Eqs. (1) and (2). Similarly the (nearly) adiabatic Floquet time evolution operator factorizes into decoupled subspaces (not labeled by $|\uparrow\downarrow\rangle$). At any finite drive frequency the evolution operator mixes these subspaces resulting in topologically trivial bands. As a result, adiabatic Thouless pumps do not continuously connect to the diabatic case discussed here; in addition, our control trajectory directly traverses the gap-closing point in the SSH model (when $J = J'$) and thus could not operate as an adiabatic pump.

Analogous schemes can create topological edge [5] and surface states [42] in 2D and 3D and are related to recently observed anomalous 2D Floquet systems [43–45]. These systems are characterized by a winding number [7] related to crystal momentum-resolved micromotion [46].

The authors thank W. D. Phillips for productive discussions, and C. W. Clark and C. A. Bracamontes for carefully reading the manuscript. This work was partially supported by the National Institute of Standards and Technology, and the National Science Foundation through the Physics Frontier Center at the Joint Quantum Institute (PHY-1430094) and the Quantum Leap Challenge Institute for Robust Quantum Simulation (OMA-2120757).

*ian.spielman@nist.gov

[1] K. von Klitzing, G. Dorda, and M. Pepper, Phys. Rev. Lett. **45**, 494 (1980).
[2] S.-C. Zhang and J. Hu, Science **294**, 823 (2001).
[3] M. Z. Hasan and C. L. Kane, Rev. Mod. Phys. **82**, 3045 (2010).
[4] P. Delplace, J. B. Marston, and A. Venaille, Science **358**, 1075 (2017).
[5] T. Kitagawa, E. Berg, M. Rudner, and E. Demler, Phys. Rev. B **82**, 235114 (2010).
[6] N. Lindner, G. Refael, and V. Galitski, Nat. Phys. **7**, 490 (2011).
[7] M. S. Rudner, N. H. Lindner, E. Berg, and M. Levin, Phys. Rev. X **3**, 031005 (2013).
[8] J. C. Budich, Y. Hu, and P. Zoller, Phys. Rev. Lett. **118**, 105302 (2017).
[9] W. P. Su, J. R. Schrieffer, and A. J. Heeger, Phys. Rev. Lett. **42**, 1698 (1979).
[10] H.-I. Lu, M. Schemmer, L. M. Aycock, D. Genkina, S. Sugawa, and I. B. Spielman, Phys. Rev. Lett. **116**, 200402 (2016).
[11] See Supplemental Material at http://link.aps.org/supplemental/10.1103/PhysRevLett.129.040402 for the effect of interactions, our numerical model, and experimental details.
[12] T. Xiao, D. Xie, W. Gou, T. Chen, T.-S. Deng, W. Yi, and B. Yan, Eur. Phys. J. D **74**, 152 (2020).
[13] These small numbers decreased the atomic density and limited unwanted scattering processes [14].
[14] G. K. Campbell, J. Mun, M. Boyd, E. W. Streed, W. Ketterle, and D. E. Pritchard, Phys. Rev. Lett. **96**, 020406 (2006).
[15] This wavelength serves to nearly minimize the spontaneous emission rate at fixed Raman coupling strength as well as cancel the state-independent scalar light shift. All uncertainties herein reflect the uncorrelated combination of single-sigma statistical and systematic uncertainties.
[16] G. Juzeliūnas and I. B. Spielman, New J. Phys. **14**, 123022 (2012).
[17] S. Trotzky, P. Cheinet, S. Fölling, M. Feld, U. Schnorrberger, A. M. Rey, A. Polkovnikov, E. A. Demler, M. D. Lukin, and I. Bloch, Science **319**, 295 (2008).
[18] R. C. Brown, R. Wyllie, S. B. Koller, E. A. Goldschmidt, M. Foss-Feig, and J. V. Porto, Science **348**, 540 (2015).
[19] The calibrated lattice parameters for each dataset and the associated simulations are tabulated in [11].
[20] Y.-J. Lin, R. L. Compton, K. Jimenez-Garcia, W. D. Phillips, J. V. Porto, and I. B. Spielman, Nat. Phys. **7**, 531 (2011).
[21] B. K. Stuhl, H.-I. Lu, L. M. Aycock, D. Genkina, and I. B. Spielman, Science **349**, 1514 (2015).
[22] These observations cannot be explained by our model, indicating the presence of distortions of the lattice potentials; we find that a weak optical lattice, for example from small retro-reflections of our Raman lasers, can explain both of these observations.
[23] Y. Zhang, T.-T. Tang, C. Girit, Z. Hao, M. C. Martin, A. Zettl, M. F. Crommie, Y. R. Shen, and F. Wang, Nature (London) **459**, 820 (2009).
[24] D. J. Thouless, Phys. Rev. B **27**, 6083 (1983).
[25] Quantum state tomography recovers the density operator, and we take its principal eigenvector as $|\psi(q,t)\rangle$. This leaves the overall wave function phase undetermined.

Because of the gauge invariance of $F(q,t)$ this phase does not affect the value of ν.

[26] E. Alba, X. Fernandez-Gonzalvo, J. Mur-Petit, J. Pachos, and J. Garcia-Ripoll, Phys. Rev. Lett. **107**, 235301 (2011).

[27] T. Fukui, Y. Hatsugai, and H. Suzuki, J. Phys. Soc. Jpn. **74**, 1674 (2005).

[28] G. H. Reid, M. Lu, A. R. Fritsch, A. M. Piñero, and I. B. Spielman, arXiv:2203.07448.

[29] A. M. Piñeiro, D. Genkina, M. Lu, and I. B. Spielman, New J. Phys. **21**, 083035 (2019).

[30] A. Valdés-Curiel, D. Trypogeorgos, Q. Y. Liang, R. P. Anderson, and I. B. Spielman, Nat. Commun. **12**, 593 (2021).

[31] To aid in filling the band, we increased the longitudinal trap frequency to $\omega_x/2\pi \approx 25$ Hz for experiments discussed in this section.

[32] H_2 in Eq. (2) of Ref. [8] differs by a factor of -1 from the SSH model; this in effect swaps the edge and center of the BZ.

[33] L. J. LeBlanc, M. C. Beeler, K. Jimenez-Garcia, A. R. Perry, S. Sugawa, R. A. Williams, and I. B. Spielman, New J. Phys. **15**, 073011 (2013).

[34] This interference arises because our initial state (aligned along the pseudospin $\mathbf{e}_z$ direction) is an equal superposition of the gapped eigenstates (aligned in the pseudospin $\mathbf{e}_x$-$\mathbf{e}_y$ plane).

[35] A. Kitaev, in *AIP Conference Proceedings*, edited by V. Lebedev and M. Feigel'man (2009), Vol. 1134, pp. 22–26, https://aip.scitation.org/toc/apc/1134/1?size=all.

[36] F. F. Fanchini, J. E. M. Hornos, and R. d. J. Napolitano, Phys. Rev. A **75**, 022329 (2007).

[37] M. Lohse, C. Schweizer, O. Zilberberg, M. Aidelsburger, and I. Bloch, Nat. Phys. **12**, 350 (2016).

[38] S. Nakajima, T. Tomita, S. Taie, T. Ichinose, H. Ozawa, L. Wang, M. Troyer, and Y. Takahashi, Nat. Phys. **12**, 296 (2016).

[39] J. Minguzzi, Z. Zhu, K. Sandholzer, A.-S. Walter, K. Viebahn, and T. Esslinger, arXiv:2112.12788.

[40] K. J. M. Schouten and V. Cheianov, Phys. Rev. A **104**, 063315 (2021).

[41] S. Malikis and V. Cheianov, arXiv:2104.02751.

[42] B. Huang, V. Novičenko, A. Eckardt, and G. Juzeliūnas, Phys. Rev. B **104**, 104312 (2021).

[43] L. J. Maczewsky, J. M. Zeuner, S. Nolte, and A. Szameit, Nat. Commun. **8**, 13756 (2017).

[44] S. Mukherjee, A. Spracklen, M. Valiente, E. Andersson, P. Öhberg, N. Goldman, and R. R. Thomson, Nat. Commun. **8**, 1 (2017).

[45] K. Wintersperger, C. Braun, F. N. Ünal, A. Eckardt, M. D. Liberto, N. Goldman, I. Bloch, and M. Aidelsburger, Nat. Phys. **16**, 1058 (2020).

[46] F. N. Ünal, A. Eckardt, and R.-J. Slager, Phys. Rev. Research **1**, 022003(R) (2019).